

Highly nonlinear biexcitonic photocurrent from ultrafast inter-layer charge transfer

Sarthak Das,[†] Garima Gupta,[†] Suman Chatterjee,[†] Kenji Watanabe,[‡] Takashi Taniguchi,[¶] and Kausik Majumdar^{*,†}

[†]*Department of Electrical Communication Engineering, Indian Institute of Science, Bangalore 560012, India*

[‡]*Research Center for Functional Materials, National Institute for Materials Science, 1-1 Namiki, Tsukuba 305-044, Japan*

[¶]*International Center for Materials Nanoarchitectonics, National Institute for Materials Science, 1-1 Namiki, Tsukuba, 305-044 Japan*

E-mail: kausikm@iisc.ac.in

Abstract

Strong Coulomb interaction in monolayer semiconductors allows them to host optically active large many-body states, such as the five-particle state, charged biexciton. Strong nonlinear light absorption by the charged biexciton under spectral resonance, coupled with its charged nature, makes it intriguing for nonlinear photodetection - an area that is hitherto unexplored. Using the high built-in vertical electric field in an asymmetrically designed few-layer graphene encapsulated 1L-WS₂ heterostructure, here we report a large, highly nonlinear photocurrent arising from the strong absorption by two charged biexciton species under zero external bias (self-powered mode). Time-resolved measurement reveals that the generated charged biexcitons transfer to the few-layer graphene in a timescale of sub-5 ps, indicating an ultrafast intrinsic limit of the photoresponse. By

using single- and two-color photoluminescence excitation spectroscopy, we show that the two biexcitonic peaks originate from bright-dark and bright-bright exciton-trion combinations. Such innate nonlinearity in the photocurrent due to its biexcitonic origin, coupled with the ultrafast response due to swift inter-layer charge transfer, exemplifies the promise of manipulating many-body effects in monolayers towards viable optoelectronic applications.

Keywords: Charged biexciton, Photocurrent spectroscopy, Photoluminescence excitation spectroscopy, Superlinear photocurrent, van der Waals heterojunction, ultrafast charge transfer.

A superlinear photodetector, where the output electrical signal varies in a superlinear manner with the input light intensity, is attractive for several functional optoelectronic applications, such as, higher harmonics generator, square-law detector, compensator for sub-linearity, optical implementation of neural circuits, and several other analog applications. However, there are very few reports to date¹⁻⁴ demonstrating a nonlinear photocurrent, and the reported degree of nonlinearity is often weak and highly dependent on the design/device parameter. A nonlinear photocurrent generation from the intrinsic nonlinear absorption of the active material will thus be highly attractive.

Reduced dielectric screening and enhanced quantum confinement lead to a high binding energy of excitonic complexes in monolayers of transition metal dichalcogenides (TMDs). The TMD monolayers thus serve as an excellent test bed to probe many-body effects in complex excitonic states.⁵⁻¹¹ The signatures of two (exciton), three (charged exciton or trion), four (biexciton) or five-particle (charged biexciton) states have been extensively probed through several optical spectroscopic techniques.⁵⁻¹⁶ These many-body states along with their different spin and valley configurations of the constituent particles further lead to a nexus of complex states.^{7,17,18} Of particular interest is the large five-particle state - charge biexciton,^{5-8,16} which dominates the optical response of monolayer WS₂ and WSe₂ at relatively higher power density because of their strong nonlinearity due to many-body effect.^{5-8,16} The charged biexciton state also exhibits large gate tunability,⁵⁻⁸ electric field induced quantum confined Stark effect,¹⁹ and magnetic field induced splitting.^{5,7} As the neutral biexcitons can be formed by both “bright-bright” and “bright-dark” excitons,^{5,6,8-10} similar configurations of exciton-trion can lead to two different types of charged biexciton formation.^{7,16} The strong nonlinear light absorption makes both these charged biexcitonic states an interesting system for nonlinear photocurrent generation - an area that has not been explored to date.

In this work, we reveal the configuration of such charged biexcitonic species in WS₂ with the

help of a combination of one- and two-color excitation spectroscopy. Using an asymmetric van der Waals heterostructure, we demonstrate a strong nonlinear photocurrent generation in self-powered mode (under zero external bias) through photo-absorption by these two types of charged biexciton, followed by their ultrafast (< 5 ps) inter-layer transfer.

Result and Discussion:

Figure 1a shows the schematic diagram of the 1L-WS₂ device (GWG) encapsulated with a thick few-layer graphene (FLG) from top and a relatively thin FLG film from the bottom (see **Methods** for fabrication details). The optical image of two such devices after completion of fabrication is shown in **Supporting Information S1**. The different thickness values of the top and bottom FLG layers, and their different dielectric environments induce a difference in doping between the two. This effect, coupled with the ultra-thin nature of the 1L-WS₂, results in a strong vertical built-in field in the WS₂ layer.^{12,20} Upon photoexcitation, this configuration allows us to obtain a photocurrent (I_{ph}) under zero external bias (V_{ext}), which has two advantages. First, the average dark current is zero, which in turn suppresses the dark noise. Second, this allows an operation in the self-powered mode without requiring any external power supply to the device. We excite the sample using a tunable source (supercontinuum laser with tunable filter from NKT Photonics), and record both I_{ph} and the photoluminescence (PL) at 4.5 K (see **Methods** for characterization setup). Note that the photocurrent away from the GWG junction is significantly suppressed (see **Supporting Information S1**).

We plot the measured photocurrent (I_{ph} in symbols) as a function of the excitation wavelength (λ) in Figure 1b. The baseline corresponds to the zero average dark current. The

value of I_{ph} is small when $\lambda > 620$ nm, suggesting that the photoresponse purely due to graphene absorption is small. The solid trace fitting the data can be decomposed into several individual peaks (shown in shaded areas). To understand the origin of the I_{ph} peaks, we compare them with the peaks obtained in the PL spectra from both the GWG portion as well as an isolated WS₂ on hBN (HW) portion (see Figure 1c-d). From the comparison, we identify that the I_{ph} peaks originate from photo-absorption by trion (X^-) around 605 nm and charged biexciton (XX_D^-) around 610 nm. Strikingly, I_{ph} spectrum does not exhibit any peak when the excitation is at the neutral exciton (X^0) resonance around 595 nm.¹² We also observe another strong peak (XX_B^-) of I_{ph} around 613 nm, which is observable both in the PL spectra from the GWG stack as well as the HW stack. We note here that the small spectral shift of the PL peaks between the GWG and the HW stacks results from Coulomb screening which causes a reduction in both the binding energy of the excitonic complexes as well as the quasiparticle bandgap.²¹⁻²³

To further identify the origin of these peaks, we measure I_{ph} as a function of the incident laser power (P) at every wavelength, and fit the obtained data as $I_{ph} \propto P^\alpha$ (Figure 1e). While the X^- peak shows a power-law exponent that is slightly less than unity ($\alpha = 0.82 \pm 0.05$), the XX_D^- and XX_B^- peaks exhibit $\alpha = 1.65 \pm 0.08$ and $\alpha = 1.8 \pm 0.2$, respectively. Under quasi-equilibrium situation, we expect that $\alpha \approx 2$ for the charged biexciton (shown later), which reduces as the system is pushed towards non-equilibrium.¹⁶ Thus, the strong non-linearity in the observed I_{ph} with the incident optical power suggests a biexcitonic origin of the two photocurrent peaks. In **Supporting Information S2**, we obtain similar results from another fabricated device, with $\alpha = 1.17 \pm 0.16$, 1.41 ± 0.14 , and 1.83 ± 0.30 for the X^- , XX_D^- , and XX_B^- species, respectively. We identify the configuration of the two charged biexcitons as depicted in Figure 1f (supported further later). Note that the observation of multiple biexcitonic peaks have been reported previously as well.⁷

Note that, while such charged biexcitons have been studied in the past through photoluminescence measurements,^{5-10,16} no direct evidence about their electronic configuration exists in literature. To explore such configuration of these biexcitonic species, we perform both one- and two-color photoluminescence excitation (PLE) spectroscopy on the isolated part of the WS₂ flake. First we scan the excitation wavelength (λ) and measure the PL intensity at the XX_D^- and XX_B^- peaks at 4.5 K, as schematically shown in Figure 2a (see **Methods** for characterization details). The bottom panel of Figure 2b shows that both the peaks exhibit strong emission when the excitation is in resonance with the X^0 peak, with the intensity of the XX_D^- being higher than the XX_B^- peak (for reference, the corresponding PL of WS₂ is shown in the top panel of Figure 2b). However, luminescence intensity is negligible for both the peaks when the excitation resonates with the X^- peak. This suggests that generating the neutral exciton is crucial to the formation of the charged biexciton, which is otherwise suppressed due to lack of formation of X^0 when only the trion (at lower energy) is generated. Further, by keeping the excitation source at the peak intensity wavelength (that is, resonant to X^0), we vary its power and record the corresponding PL intensity of $XX_{B,D}^-$ (Figure 2c). The power dependent PL intensity again follows a power-law with $\alpha = 1.62 \pm 0.04$ and 1.96 ± 0.05 for XX_D^- and XX_B^- peaks, respectively, which are in good agreement with the I_{ph} power-law.

To further verify the nature of the charged biexcitons, we next use a two-color excitation spectroscopy where we keep one excitation wavelength (λ_1) fixed at X^0 resonance and scan the wavelength (λ_2) of the other excitation, as schematically shown in Figure 2d (see **Methods**). We observe in Figure 2e that, for the XX_D^- peak, the strongest intensity remains when λ_2 also resonates with the X^0 peak. However, we also observe a non-zero luminescence intensity when λ_2 is around the X^- peak, unlike the previous single wavelength PLE experiment. On the other hand, for the XX_B^- peak, we notice distinct peaks when λ_2 is close to both X^0 and X^- resonance, both being comparable in intensity (shown in Figure 2e). In

particular, the formation of the XX_B^- through the simultaneous absorption of X^0 (through λ_1 in green) and X^- (through λ_2 in red) is schematically shown in Figure 2d. These observations point to the fact that both XX_D^- and XX_B^- species originate from a combination of X^0 and X^- , suggesting their charged biexcitonic nature. This is in good agreement with the gate voltage dependence of the PL intensity of the two peaks, measured with a 532 nm continuous wave laser excitation (See **Supporting Information S3**). With an increase in the positive or negative gate voltage, the intensity of both the peaks increases due to gate voltage induced doping. This is in good agreement with previous reports as well,^{5,8} and supports their charged biexcitonic nature.

Based on the above observations, we propose that XX_D^- is formed through the combination of a bright neutral exciton (X_B^0) and a dark trion (X_D^-), as reported previously^{5,8,16} (see left panel of Figure 1f). On the other hand, XX_B^- originates from X_B^0 and a bright trion (X_B^-), as shown in the right panel of Figure 1f. The long-lived nature of X_D^- results in a higher population density of XX_D^- , and hence a stronger PL intensity, compared with XX_B^- . As indicated by the dashed lines in Figure 2a, the bright excitons, upon generation, relax to the lower energy dark states by undergoing inter-valley scattering. This explains the reason for XX_D^- showing a strong intensity when λ is close to the neutral exciton resonance. This intensity reduces for the XX_B^- case due to quick loss of X_B^0 to the lower energy dark states.

Interestingly, while the XX_B^- is of higher energy than XX_D^- , the corresponding transition energy (for both absorption and emission) is less for XX_B^- (Figure 1b-d). This is schematically explained in Figure 2f. The configuration of the two different charged biexcitons in Figure 1f indicates that $E_{X_B^-} - E_{X_D^-} = \Delta_c + \chi$, and $E_{XX_B^-} - E_{XX_D^-} = \Delta_c + \chi'$, where Δ_c and χ (χ') denote the spin-orbit splitting in the conduction bands, and the exchange energy of the trion (charged biexciton) state. Due to an enhanced screening, we expect a reduced wave function overlap in the charged biexciton compared with the trion, and hence $\chi' < \chi$. The

transition energy difference between the two species corresponds to $\hbar\omega_{XX_D^-} - \hbar\omega_{XX_B^-} = \chi - \chi'$, which is ~ 12 meV.

After establishing that the two strong photoluminescence peaks around 610 and 613 nm originating from XX_D^- and XX_B^- , respectively, we now focus on the mechanism that causes the I_{ph} , as explained in Figure 3. Note that, the top and bottom FLG layers can absorb the light resulting in injection of hot electrons and holes from both the FLG layers to WS_2 . However, due to the large band offset between WS_2 and FLG on both sides of WS_2 , these hot carriers can move towards either direction, preventing any significant net flow of charge along one direction (Figure 3a). This suppresses the net I_{ph} purely due to FLG absorption, as observed for $\lambda > 620$ nm in Figure 1b. We observe that photon absorption by multi-particle states in WS_2 clearly enhances I_{ph} . As the I_{ph} is obtained under zero external bias, it relies on the vertical built-in field in WS_2 . However, note that the built-in field is not strong enough to dissociate the strongly bound exciton and other higher order states into individual electrons and holes. The photocurrent is thus suppressed when the excitation is in resonance with the charge neutral exciton (see Figure 1b).

We first ask the question: what is generation mechanism of the charged biexcitons through resonant absorption of photons that is responsible for the observed I_{ph} ? There are two possibilities, namely (1) two-photon absorption (TPA),²⁴⁻²⁶ and (2) absorption of a photon that promotes an already prepared bright or dark trion state to the corresponding charged biexciton state. The TPA process is schematically shown in Figure 3b. We expect that the two-photon absorption, which occurs through a virtual state (indicated by the dashed line in Figure 3b), is a relatively weak process. In addition, energy conservation dictates that in the TPA process, the photo-absorption must occur at an energy equal to $0.5(\hbar\omega_{XX_{B,D}^-} + \hbar\omega_{X_{B,D}^-})$. However, our experimental observation suggests that the I_{ph} peaks almost exactly match with the charged biexcitons emission peaks. We thus conclude that the TPA process is not the primary mechanism for the observed photocurrent, and the latter mechanism plays a more

important role.

Since charged biexciton transition energy ($\hbar\omega_{XX_{B,D}^-}$) is lower than the trion transition energy ($\hbar\omega_{X_{B,D}^-}$), we rule out the generation of a trion via direct absorption by the WS₂ layer at an excitation energy resonant with the $\hbar\omega_{XX_{B,D}^-}$. Instead, hot electrons and holes are generated in the top and bottom FLG layers at these excitation wavelengths due to broad-band absorption arising from broad joint density of states in FLG.²⁷⁻²⁹ These hot carriers are injected into the WS₂ layer through ultrafast inter-layer charge transfer.^{3,30,31} Note that, while the electron-hole recombination time is short in FLG,^{32,33} the fast out-of-plane transfer timescale allows such hot carrier transfer to WS₂ before they recombine in the FLG films.³⁴ These non-equilibrium hot electrons and holes occupy the bands of both valleys in WS₂, helping to prepare the initial bright and dark trion state (left panel of Figure 3c). The excitation pulse width (~ 60 ps) is much larger than the inter-layer charge transfer. Hence, another photon absorption (within the same pulse) with an energy equal to $\hbar\omega_{XX_{B,D}^-}$ promotes the respective trion state to the corresponding charged biexciton state ($XX_{B,D}^-$), as schematically shown in Figure 3d. We must note that these two processes can happen resonantly as well, which reduces the effective energy barrier for carrier injection from FLG to WS₂ due to the Coulomb interaction arising from the many-body effect.

As argued earlier, the hot electrons and holes injected from top and bottom FLG to WS₂ do not individually contribute to a large I_{ph} due to a lack of strong asymmetry (Figure 3a). However, when the injected electron or hole is bound to the fat many-body particle, the probability of movement towards either side is suppressed. Instead, the charged many-body particle itself is dragged by the built-in field, helping in generating a net photocurrent (see Figure 3d). In addition, when the incoming photon is in resonance with one of the charged many-body states (like trion or charged biexciton), the hot carriers while being injected from FLG, “feel” the many-body Coulomb interaction, and encounters a smaller injection

barrier height, resonantly forming the many-body state. Thus the many-body state acts like an intermediate state that carries the net charge from the top FLG to the bottom FLG film, thus allowing the flow of a net photocurrent conserving the charge.

The right panel of Figure 3c schematically illustrates another possible way the initial bright or dark trion state can be prepared is by direct inter-layer photon absorption,³⁰ where an electron in the valence band of WS₂ (FLG) is promoted to the conduction band of FLG (WS₂), leaving behind a hole. Our experimental observations do not distinguish between these two different mechanisms of initial trion state preparation, and both processes can contribute to the measured I_{ph} .

In order to establish the role of FLG in supplying the carriers to form the charge biexcitonic states, we fabricate a lateral hBN capped WS₂ device, and measure the lateral photocurrent by exciting the laser spot at the middle of the channel (see **Supporting Information S4**). The first striking observation is that the total photocurrent is nearly 1000-fold less in the lateral device, compared with the vertical GWG device. Second, the total photocurrent at the exciton and charged biexciton excitation are similar, unlike the GWG vertical device. Such strong relative suppression of I_{ph} at the charged biexciton excitation energy suggests that the formation of charged biexciton is less efficient without the presence of the FLG.

The two-step mechanism of the generation of the biexcitonic current in the GWG device presented above can be modelled using a simple rate equation:

$$\frac{dn_{XX^-}}{dt} = \gamma n_{X^-} P - \frac{n_{XX^-}}{\tau} \quad (1)$$

Here, n_{XX^-} and n_{X^-} are respectively the charged biexciton and trion population, P is the optical power, γ is a proportionality constant, and τ is the net lifetime of the charged

biexciton in the GWG stack. The first term on the right hand side in Equation 1 takes care of the initial trion state formation followed by promotion to a charged biexciton state. From the top panel of Figure 1(e), we note that $n_{X^-} \propto P^{0.82}$. Hence, using $\frac{dn_{XX^-}}{dt} = 0$ under steady state, we obtain

$$I_{ph} \propto n_{XX^-} \propto P^{1.82} \quad (2)$$

which is in good agreement with the superlinear power law observed at the charged biexciton resonance in the middle and bottom panels of Figure 1(e).

To estimate the timescale of the photocurrent generation mechanism, we compare the net lifetime of the charged biexciton in HW and GWG stacks by measuring time-resolved photoluminescence (TRPL) of the charged biexciton peak (see **Methods** for measurement details). The results are provided in Figure 4. In both cases, we are able to fit the charged biexciton population (n) decay using two exponentials: $n(t) = A_1 e^{-t/\tau} + A_2 e^{-t/\tau_d}$, with A_1/A_2 being about an order of magnitude. The weaker component arises from the tail of the defect peak, with a slow timescale of τ_d , as observed in the PL spectrum from the GWG stack in Figure 1c. We focus on the stronger (and faster) decay component here, which varies from $\tau = 17.8 \pm 0.9$ ps on the HW stack to $\tau = 4.2 \pm 0.7$ ps on the GWG stack. The net lifetime (τ) of the charged biexciton can be written as

$$\frac{1}{\tau} = \Gamma_r + \Gamma_{nr} \quad (3)$$

where Γ_r and Γ_{nr} are respectively the radiative and non-radiative decay rates. Due to graphene induced screening, Γ_r is expected to be reduced in the GWG stack compared to the HW stack.³⁵ Hence, $\frac{1}{\Gamma_r} > 17.8$ ps in the GWG stack, which in turn indicates $\frac{1}{\Gamma_{nr}} < 5.4$ ps (from Equation 3). Note that, Γ_{nr} is primarily dominated by the ultrafast inter-layer charge transfer in the GWG stack,^{31,35,36} and in turn, is responsible for the photocurrent. The strong reduction of τ in the GWG stack compared with the HW stack is thus clearly due to

such fast inter-layer charge transfer induced enhanced Γ_{nr} . Such enhanced Γ_{nr} in the GWG stack is further supported by the simultaneous observation of the reduced PL counts and a reduced net lifetime of the charged biexciton. This analysis thus suggests that the generated charged biexciton transfers to graphene in a timescale of < 5.4 ps, indicating the ultrafast nature of the intrinsic photocurrent generation. Note that, the mobility and dimensions of the lateral few-layer graphene access regions, and the contact resistance at the interfaces between the few-layer graphene and metal pad contribute to the parasitic resistance of the device. Thus, while the intrinsic response is in picoseconds, the photocurrent could be eventually limited by the time constant of the entire circuit arising from the parasitic resistance and capacitance.

Conclusions

In summary, we demonstrate strong photocurrent generation under zero external bias from resonant absorption by two different five-particle charged biexciton states, followed by their ultrafast inter-layer transfer. The biexcitonic photocurrent is highly nonlinear (near-square-law) with the incident optical power and is significantly stronger than the photocurrent resulting from resonant absorption by the neutral exciton and trion. Further, the nature of the different biexcitonic species are revealed by an interesting single- and two-color photoluminescence excitation scans. Such ultrafast, narrow-band, nonlinear photodetection is promising for several applications such as higher harmonics generation of the modulating signal, receiver design in microwave photonics and visible light communication, square-law circuits, and also in nonlinear optoelectronic applications such as neural circuits. In addition, the techniques used here have intriguing prospects towards alternative spectroscopic techniques for exploring and manipulating many-body states in monolayer semiconductors

and beyond.

Methods

Device fabrication: We prepare the GWG heterostructure devices using sequential dry-transfer method where the individual layers were exfoliated from bulk crystals onto Polydimethylsiloxane (PDMS) using Nitto tape. The entire stack of FLG-capped monolayer WS₂ is made on top of Si substrate covered with 285 nm SiO₂. The pre-patterned metal electrodes are prepared using photolithography followed by sputtering of Ni/Au (10/50 nm) and lift-off. The deterministic transfer of layers using micromanipulator ensures that one end of the graphite layers is placed on top the metal pads. After completion of the transfer process, the devices are annealed inside a vacuum chamber (10^{-6} mbar) at 200°C for 3 hours for better adhesion of the layers.

Scanning photocurrent and PLE measurement: For the photocurrent measurement, we excite the sample using a supercontinuum laser source cascaded with a multi-channel acousto-optic tunable filter (NKT Photonics). The laser has a repetition rate of 78 MHz, and the individual pulses have a width of ~ 60 ps. The light is focused on top of the heterojunction using a $\times 50$ long-working-distance objective (numerical aperture of 0.5) through an optical window while keeping the device inside a closed-cycle cryostat chamber at 4.5 K. The power values reported here are measured before the objective using a commercial silicon photodetector (from Edmund Optics), which has a linear response in the range of the measured power values. We record the photocurrent under zero external bias using a Keithley 2636B SMU. The photoluminescence excitation (PLE) spectroscopy is performed by exciting the sample with the same tunable source (linewidth ~ 0.5 nm). The emitted photons are directed to a spectrometer after passing through a bandpass filter with the

central wavelength at 610 nm and an FWHM of 10 nm. For the two-color excitation, we select two wavelengths from the tunable filter by choosing two different channels, and other components of the setup remain the same as the single-wavelength excitation. A schematic diagram of the measurement setup is shown in **Supporting Information S5**.

TRPL measurement: We use a 531 nm pulsed laser (PicoQuant) controlled by the PDL 800-D driver (with a pulse width of ~ 40 ps and a repetition rate of 10 MHz) for the TRPL measurement. The emission signal is connected to a single photon counting avalanche detector from Micro Photon Devices (SPD-050-CTC). The detector is further connected to a Time-Correlated Single Photon Counting (TCSPC) system (PicoHarp 300 from PicoQuant). We have used a combination of a 600 nm longpass filter and a 610 nm bandpass (FWHM 10 nm) to collect the emitted photon from the charged biexciton states. The FWHM of the instrument response function (IRF) is 52 ps. We perform the deconvolution using QuCoa software (PicoQuant) that allows us to accurately extract timescale down to 10% of the IRF width.³⁷

SUPPLEMENTARY INFORMATION

The Supporting Information is available free of charge at XXX.

Optical image and low temperature photoluminescence; photocurrent from device-2; gate dependent photoluminescence of 1L-WS₂ at $T = 4.5$ K; photoluminescence and photocurrent characteristics from a lateral device; schematic of experimental setup.

ACKNOWLEDGMENTS

K.M. acknowledges useful discussion with Varun Raghunathan. This work was supported in part by a Core Research Grant from the Science and Engineering Research Board (SERB) under Department of Science and Technology (DST), a grant from Indian Space Research Organization (ISRO), a grant from MHRD under STARS, and a grant from MHRD, MeitY and

DST Nano Mission through NNetRA. K.W. and T.T. acknowledge support from the Elemental Strategy Initiative conducted by the MEXT, Japan (Grant Number JPMXP0112101001) and JSPS KAKENHI (Grant Numbers 19H05790, 20H00354 and 21H05233).

Author Contribution

K.M. designed the experiment. S.D. and S.C. fabricated the devices. K.W. and T.T. provided the hBN flakes. S.D., G.G., and K.M. performed the measurements. S.D., G.G., S.C. and K.M. contributed to the analysis of the data and writing of the paper. S.D. and G.G. contributed equally to this work.

Competing Interests

The Authors declare no Competing Financial or Non-Financial Interests.

Data Availability

Data available on reasonable request from the corresponding author.

References

- (1) Klee, V.; Preciado, E.; Barroso, D.; Nguyen, A. E.; Lee, C.; Erickson, K. J.; Triplett, M.; Davis, B.; Lu, I.-H.; Bobek, S., et al. Superlinear Composition-Dependent Photocurrent in CVD-Grown Monolayer $\text{MoS}_{2(1-x)}\text{Se}_{2x}$ Alloy Devices. *Nano Letters* **2015**, *15*, 2612–2619.
- (2) Ma, Q.; Andersen, T. I.; Nair, N. L.; Gabor, N. M.; Massicotte, M.; Lui, C. H.; Young, A. F.; Fang, W.; Watanabe, K.; Taniguchi, T., et al. Tuning Ultrafast Electron

- Thermalization Pathways in a van der Waals Heterostructure. *Nature Physics* **2016**, *12*, 455–459.
- (3) Massicotte, M.; Schmidt, P.; Vialla, F.; Watanabe, K.; Taniguchi, T.; Tielrooij, K.-J.; Koppens, F. H. Photo-Thermionic Effect in Vertical Graphene Heterostructures. *Nature Communications* **2016**, *7*, 1–7.
- (4) Dandu, M.; Gupta, G.; Majumdar, K. Negative Differential Photoconductance as a Signature of Nonradiative Energy Transfer in van der Waals Heterojunction. *ACS Nano* **2021**, *15*, 16432–16441.
- (5) Ye, Z.; Waldecker, L.; Ma, E. Y.; Rhodes, D.; Antony, A.; Kim, B.; Zhang, X.-X.; Deng, M.; Jiang, Y.; Lu, Z., et al. Efficient Generation Of Neutral and Charged Biexcitons in Encapsulated WSe₂ Monolayers. *Nature Communications* **2018**, *9*, 1–6.
- (6) Chen, S.-Y.; Goldstein, T.; Taniguchi, T.; Watanabe, K.; Yan, J. Coulomb-Bound Four-and Five-Particle Intervalley States in an Atomically-Thin Semiconductor. *Nature Communications* **2018**, *9*, 1–8.
- (7) Zinkiewicz, M.; Wozniak, T.; Kazimierzuk, T.; Kapuscinski, P.; Oreszczuk, K.; Grzeszczyk, M.; Bartos, M.; Nogajewski, K.; Watanabe, K.; Taniguchi, T., et al. Excitonic Complexes in n-doped WS₂ Monolayer. *Nano Letters* **2021**, *21*, 2519–2525.
- (8) Barbone, M.; Montblanch, A. R.-P.; Kara, D. M.; Palacios-Berraquero, C.; Cadore, A. R.; De Fazio, D.; Pingault, B.; Mostaani, E.; Li, H.; Chen, B., et al. Charge-Tuneable Biexciton Complexes in Monolayer WSe₂. *Nature Communications* **2018**, *9*, 1–6.
- (9) Steinhoff, A.; Florian, M.; Singh, A.; Tran, K.; Kolarczik, M.; Helmrich, S.; Achstein, A. W.; Woggon, U.; Owschimikow, N.; Jahnke, F., et al. Biexciton Fine Structure in Monolayer Transition Metal Dichalcogenides. *Nature Physics* **2018**, *14*, 1199–1204.

- (10) Hao, K.; Specht, J. F.; Nagler, P.; Xu, L.; Tran, K.; Singh, A.; Dass, C. K.; Schüller, C.; Korn, T.; Richter, M., et al. Neutral and Charged Inter-Valley Biexcitons in Monolayer MoSe₂. *Nature Communications* **2017**, *8*, 1–7.
- (11) Paur, M.; Molina-Mendoza, A. J.; Bratschitsch, R.; Watanabe, K.; Taniguchi, T.; Mueller, T. Electroluminescence from Multi-Particle Exciton Complexes in Transition Metal Dichalcogenide Semiconductors. *Nature Communications* **2019**, *10*, 1–7.
- (12) Kallatt, S.; Das, S.; Chatterjee, S.; Majumdar, K. Interlayer Charge Transport Controlled by Exciton–Trion Coherent Coupling. *npj 2D Materials and Applications* **2019**, *3*, 1–8.
- (13) Jadczyk, J.; Bryja, L.; Kutrowska-Girzycka, J.; Kapuściński, P.; Bieniek, M.; Huang, Y.-S.; Hawrylak, P. Room Temperature Multi-Phonon Upconversion Photoluminescence in Monolayer Semiconductor WS₂. *Nature Communications* **2019**, *10*, 1–10.
- (14) Mostaani, E.; Szyniszewski, M.; Price, C.; Maezono, R.; Danovich, M.; Hunt, R.; Drummond, N.; Fal’Ko, V. Diffusion Quantum Monte Carlo Study Of Excitonic Complexes in Two-Dimensional Transition-Metal Dichalcogenides. *Physical Review B* **2017**, *96*, 075431.
- (15) Rodin, A.; Trushin, M.; Carvalho, A.; Neto, A. C. Collective Excitations in 2D Materials. *Nature Reviews Physics* **2020**, *2*, 524–537.
- (16) Chatterjee, S.; Das, S.; Gupta, G.; Watanabe, K.; Taniguchi, T.; Majumdar, K. Probing Biexciton In Monolayer WS₂ Through Controlled Many-Body Interaction. *2D Materials* **2022**, *9*, 015023.
- (17) Liu, E.; van Baren, J.; Liang, C.-T.; Taniguchi, T.; Watanabe, K.; Gabor, N. M.; Chang, Y.-C.; Lui, C. H. Multipath Optical Recombination Of Intervalley Dark Excitons and Trions in Monolayer WSe₂. *Physical Review Letters* **2020**, *124*, 196802.

- (18) Li, Z.; Wang, T.; Jin, C.; Lu, Z.; Lian, Z.; Meng, Y.; Blei, M.; Gao, S.; Taniguchi, T.; Watanabe, K., et al. Emerging Photoluminescence from the Dark-Exciton Phonon Replica in Monolayer WSe₂. *Nature Communications* **2019**, *10*, 1–7.
- (19) Abraham, N.; Watanabe, K.; Taniguchi, T.; Majumdar, K. Anomalous Stark Shift of Excitonic Complexes in Monolayer WS₂. *Physical Review B* **2021**, *103*, 075430.
- (20) Kim, C. O.; Kim, S.; Shin, D. H.; Kang, S. S.; Kim, J. M.; Jang, C. W.; Joo, S. S.; Lee, J. S.; Kim, J. H.; Choi, S.-H., et al. High Photoresponsivity in An All-Graphene P-N Vertical Junction Photodetector. *Nature Communications* **2014**, *5*, 1–7.
- (21) Ugeda, M. M.; Bradley, A. J.; Shi, S.-F.; Felipe, H.; Zhang, Y.; Qiu, D. Y.; Ruan, W.; Mo, S.-K.; Hussain, Z.; Shen, Z.-X., et al. Giant Bandgap Renormalization and Excitonic Effects in a Monolayer Transition Metal Dichalcogenide Semiconductor. *Nature Materials* **2014**, *13*, 1091–1095.
- (22) Raja, A.; Chaves, A.; Yu, J.; Arefe, G.; Hill, H. M.; Rigosi, A. F.; Berkelbach, T. C.; Nagler, P.; Schüller, C.; Korn, T., et al. Coulomb Engineering of the Bandgap and Excitons in Two-Dimensional Materials. *Nature Communications* **2017**, *8*, 1–7.
- (23) Gupta, G.; Kallatt, S.; Majumdar, K. Direct Observation of Giant Binding Energy Modulation of Exciton Complexes in Monolayer MoSe₂. *Physical Review B* **2017**, *96*, 081403.
- (24) Kamada, H.; Ando, H.; Temmyo, J.; Tamamura, T. Excited-State Optical Transitions Of Excitons and Biexcitons In A Single In_XGa_{1-X} As Quantum Disk. *Physical Review B* **1998**, *58*, 16243.
- (25) Yamada, Y.; Ueki, Y.; Nakamura, K.; Taguchi, T.; Ishibashi, A.; Kawaguchi, Y.; Yokogawa, T. Stokes Shift Of Biexcitons In Al_XGa_{1-X} N Epitaxial Layers. *Physical Review B* **2004**, *70*, 195210.

- (26) Yamamoto, A.; Miyajima, K.; Goto, T.; Ju Ko, H.; Yao, T. Biexciton Luminescence In High-Quality ZnO Epitaxial Thin Films. *Journal of Applied Physics* **2001**, *90*, 4973–4976.
- (27) Bassani, F.; Parravicini, G. P. Band Structure and Optical Properties Of Graphite and Of The Layer Compounds GaS and GaSe. *Il Nuovo Cimento B (1965-1970)* **1967**, *50*, 95–128.
- (28) Johnson, L. G.; Dresselhaus, G. Optical Properties of Graphite. *Physical Review B* **1973**, *7*, 2275.
- (29) Pedersen, T. G. Analytic Calculation of the Optical Properties of Graphite. *Physical Review B* **2003**, *67*, 113106.
- (30) Yuan, L.; Chung, T.-F.; Kuc, A.; Wan, Y.; Xu, Y.; Chen, Y. P.; Heine, T.; Huang, L. Photocarrier Generation From Interlayer Charge-Transfer Transitions In WS₂-Graphene Heterostructures. *Science Advances* **2018**, *4*, e1700324.
- (31) Fu, S.; du Fossé, I.; Jia, X.; Xu, J.; Yu, X.; Zhang, H.; Zheng, W.; Krasel, S.; Chen, Z.; Wang, Z. M., et al. Long-Lived Charge Separation Following Pump-Wavelength-Dependent Ultrafast Charge Transfer in Graphene/WS₂ Heterostructures. *Science Advances* **2021**, *7*, eabd9061.
- (32) George, P. A.; Strait, J.; Dawlaty, J.; Shivaraman, S.; Chandrashekar, M.; Rana, F.; Spencer, M. G. Ultrafast Optical-Pump Terahertz-Probe Spectroscopy of the Carrier Relaxation and Recombination Dynamics in Epitaxial Graphene. *Nano Letters* **2008**, *8*, 4248–4251.
- (33) Rana, F.; George, P. A.; Strait, J. H.; Dawlaty, J.; Shivaraman, S.; Chandrashekar, M.; Spencer, M. G. Carrier Recombination and Generation Rates For Intravalley and Intervalley Phonon Scattering in Graphene. *Physical Review B* **2009**, *79*, 115447.

- (34) Murali, K.; Abraham, N.; Das, S.; Kallatt, S.; Majumdar, K. Highly Sensitive, Fast Graphene Photodetector With Responsivity $> 10^6$ A/W Using a Floating Quantum Well Gate. *ACS Applied Materials & Interfaces* **2019**, *11*, 30010–30018.
- (35) Gupta, G.; Watanabe, K.; Taniguchi, T.; Majumdar, K. Observation Of Perfect Valley Coherence in Monolayer MoS₂ through Giant Enhancement of Exciton Coherence Time. *arXiv preprint arXiv:2106.03359* **2021**,
- (36) Lorchat, E.; López, L. E. P.; Robert, C.; Lagarde, D.; Froehlicher, G.; Taniguchi, T.; Watanabe, K.; Marie, X.; Berciaud, S. Filtering the Photoluminescence Spectra Of Atomically Thin Semiconductors With Graphene. *Nature Nanotechnology* **2020**, *15*, 283–288.
- (37) Becker, W. In *Advanced Time-Correlated Single Photon Counting Techniques*; A. W. Castleman, W. Z., J.P. Toennies, Ed.; Springer Berlin, Heidelberg, 2005; Vol. 81.

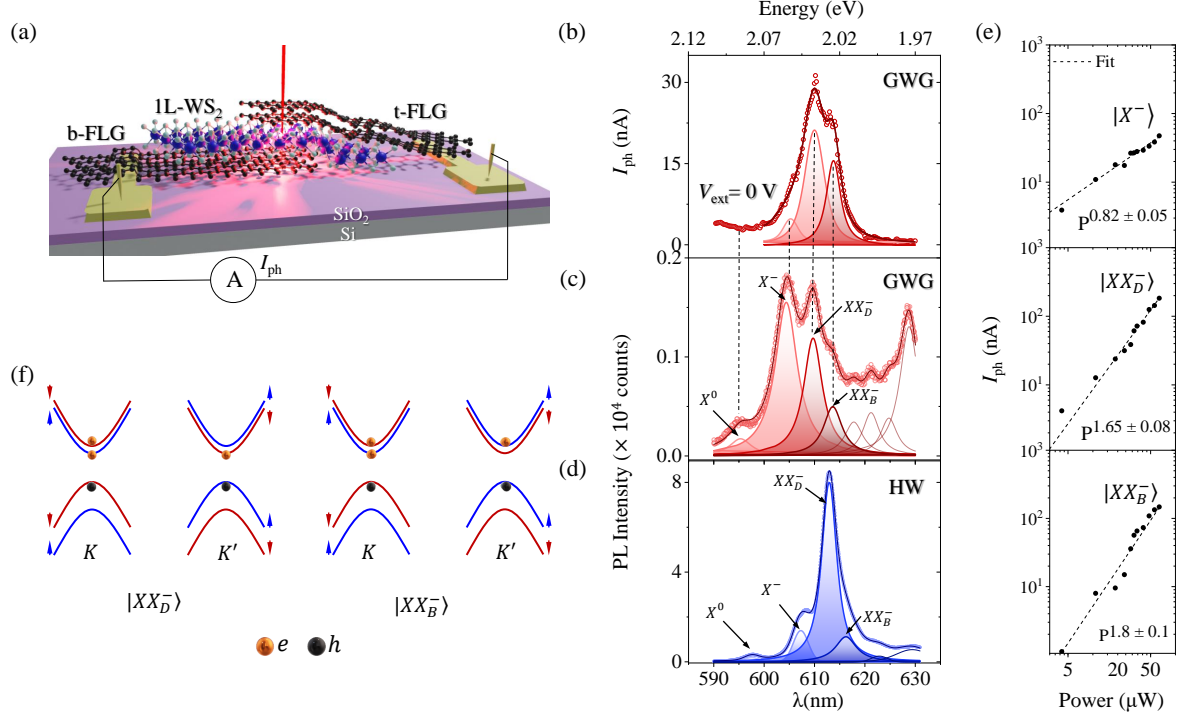


Figure 1: **Photocurrent from charged biexciton states.** (a) Schematic diagram of the 1L-WS₂ device (GWG) encapsulated with few-layer graphene from top (t-FLG) and bottom (b-FLG). The photocurrent (I_{ph}) is measured in a short-circuit configuration with zero external bias. (b) I_{ph} as a function of the excitation wavelength (λ) at $T = 4.5$ K. The spectroscopic response is decomposed into individual trion (X^-) and charged biexciton ($XX_{B,D}^-$) peaks. (c-d) Photoluminescence (PL) intensity of 1L-WS₂ from the GWG portion (c) and WS₂ on hBN (HW) portion (d). The vertical dashed lines indicate that the I_{ph} peaks match well with the PL peaks. The small shift between the GWG and HW PL peaks arise from different dielectric environment. (e) Optical power dependent I_{ph} for the X^- , XX_D^- and XX_B^- states (symbols). The fitted trend ($I_{ph} \propto P^\alpha$) is shown in dashed lines. (f) Schematic representation of the configuration of dark (XX_D^-) and bright (XX_B^-) charged biexciton states.

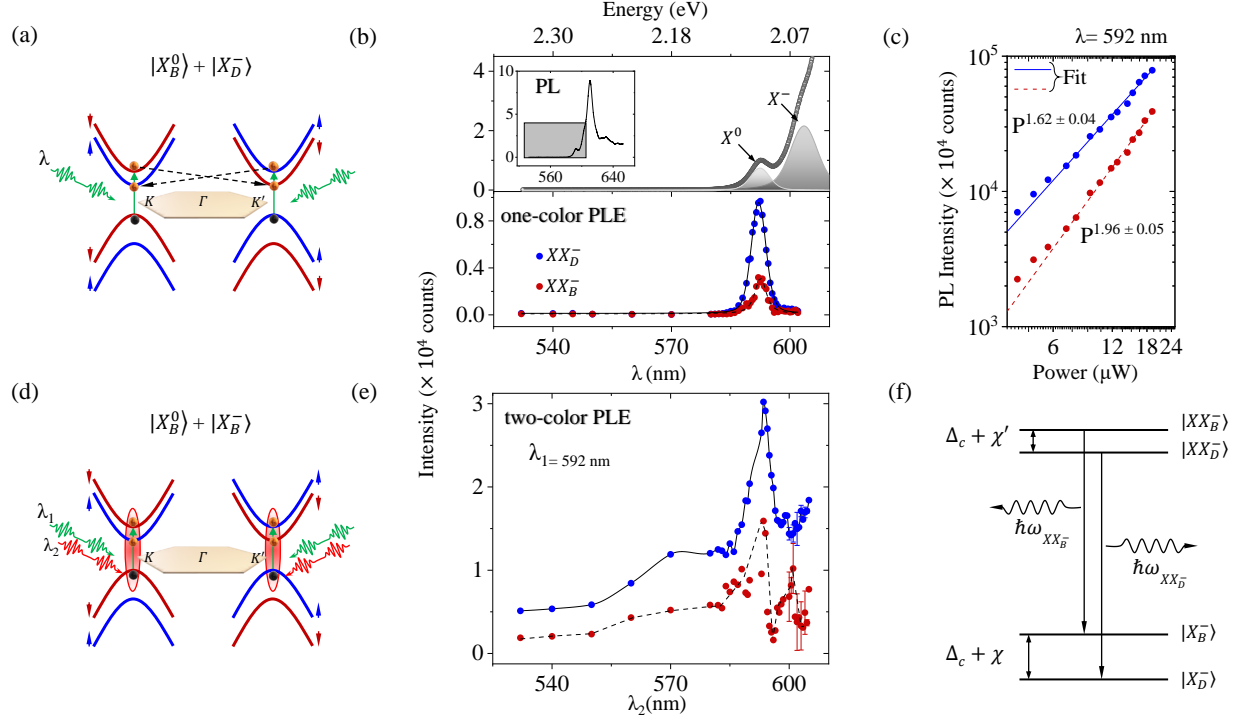


Figure 2: **One- and two-color photoluminescence excitation spectroscopy of charged biexcitons.** (a) Schematic diagram of the one-color photoluminescence excitation (PLE) spectroscopy. The dashed lines indicate the formation of lower energy dark states when the excitation is in resonance with neutral bright exciton. (b) Top panel: Zoomed-in PL spectrum for WS₂ showing the X^0 and X^- peak, with the full spectrum in the inset. Bottom panel: Emission intensity of the XX_D^- (blue symbol) and XX_B^- (red symbol) states, as a function of the excitation wavelength (energy) in the bottom (top) axis. Both of them show a pronounced emission when excitation wavelength (λ) matches with the X^0 . The solid and dashed lines are guide to eye for the XX_D^- and XX_B^- one-color PLE intensity, respectively. (c) Power dependent PL intensity of the charged biexcitons ($XX_{B,D}^-$) with excitation wavelength at 592 nm (X^0 resonance). The solid and dashed lines represent the power law fits. (d) Schematic diagram of the two-color PLE, where λ_1 is kept fixed at X^0 resonance, and λ_2 is scanned. The specific situation of λ_2 matching the trion state is highlighted. (e) PLE intensity for a two-color PLE for XX_D^- (blue symbol) and XX_B^- (red symbol). (f) Transition energy diagram corresponding to the $XX_{B,D}^-$ states. Here Δ_c and χ (χ') denote the spin-orbit splitting in the conduction bands, and the exchange energy of the trion (charged biexciton) state.

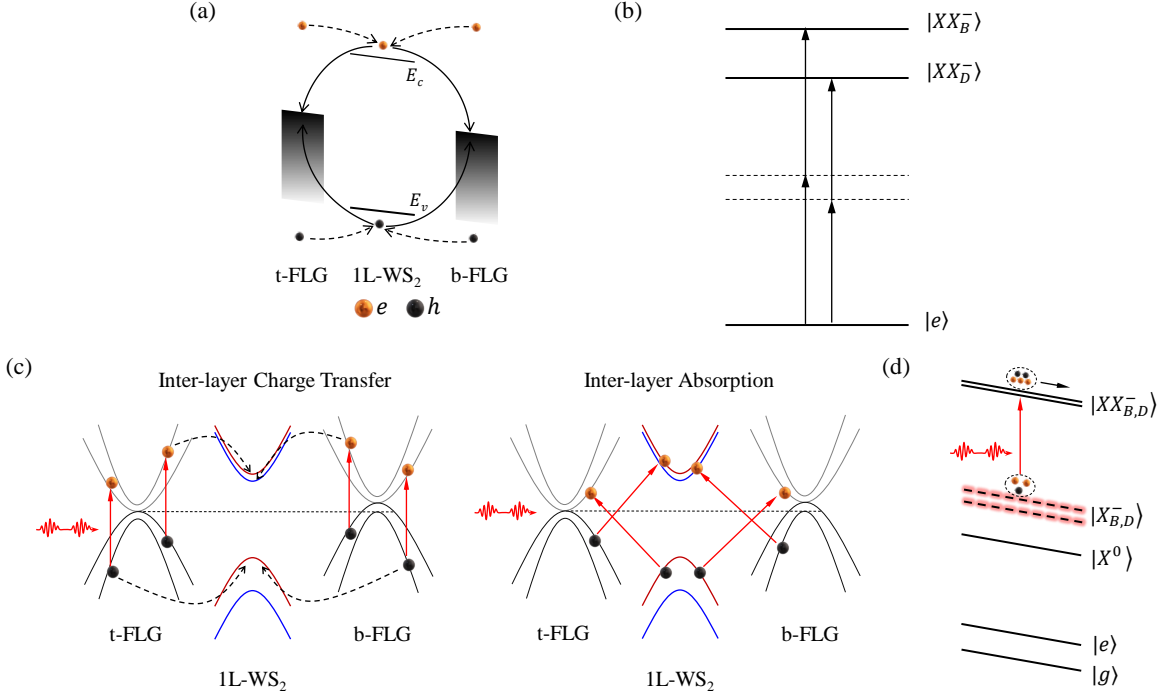


Figure 3: **Mechanism of I_{ph} generation through charged biexcitons.** (a) The light absorbed by top and bottom FLG layers results in injection of hot electrons and holes from both the FLG layers to WS₂ (dashed arrow). However, due to the large band offset between WS₂ and FLG on both sides of WS₂, these hot carriers can move towards either direction (solid arrow), hence suppress the I_{ph} . (b) Schematic of the two-photon absorption (TPA) process where energy conservation indicates that in the TPA, the photo-absorption must occur at an energy equal to $0.5(\hbar\omega_{XX_{B,D}^-} + \hbar\omega_{X_{B,D}^-})$. The dashed lines indicate the virtual states. (c) Left panel: Hot electrons and holes generated in the top and bottom FLG layers are injected into 1L-WS₂. These non-equilibrium hot electrons and holes occupy the bands of both valleys in WS₂ that eventually prepare the initial bright and dark trion state. Right panel: Generation of carriers through inter-layer photon absorption. (d) The incoming photons of 610 and 613 nm couple with the $X_{B,D}^-$ state to form the $XX_{B,D}^-$. This many body state acts like an intermediate state that carries a net charge from top FLG film to the bottom. The fat particle $XX_{B,D}^-$ reduces the probability of bidirectional movement and is dragged by the built-in vertical field, contributing to the I_{ph} .

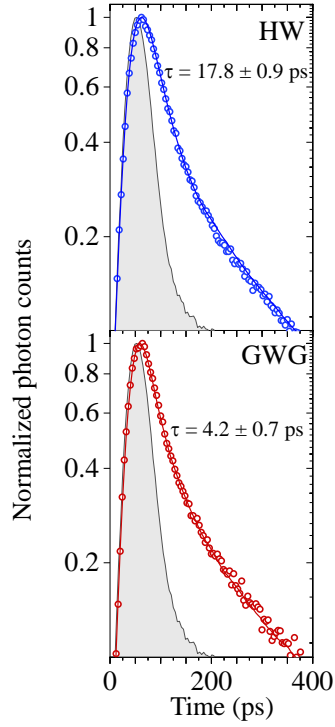


Figure 4: **Time-resolved photoluminescence measurement.** Lifetime of the charged biexciton in (a) HW and (b) GWG stacks measured via time-resolved photoluminescence (TRPL). While the decay time is 17.8 ± 0.9 ps on the HW stack, it is 4.2 ± 0.7 ps on GWG stack, indicating a faster nonradiative decay of the charged biexciton resulting from inter-layer transfer.

Supporting Information S1

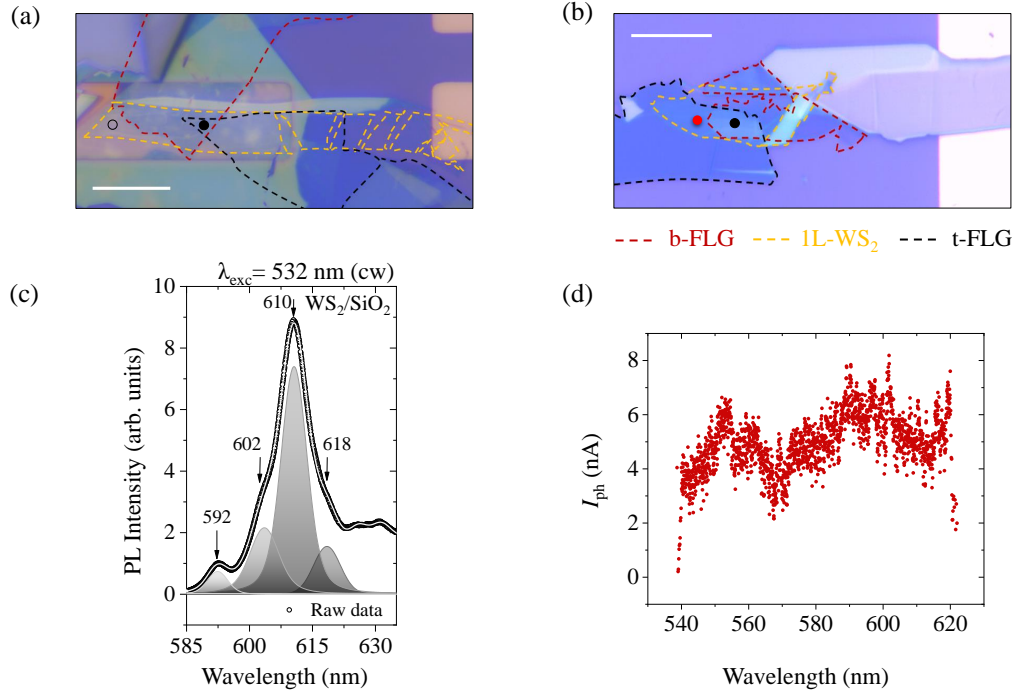


Figure 1: **Optical image and low temperature photoluminescence.** (a-b) Optical image of (a) device 1 and (b) device 2. The experimental results obtained from device 1 are presented in the main text. The experimental results from device 2 are shown in **Supporting Information S2**. The black dots represent the GWG portion in both the devices, and the open circle in (a) represents the HW portion. Boundary of the different materials are delineated with the dashed lines. Scale bar is $5 \mu\text{m}$. (c) PL spectra at $T = 4.5 \text{ K}$ for 1L-WS₂ on SiO₂ indicating the X^0 , X^- , and $XX_{B,D}^-$ peaks. (d) I_{ph} away from the junction [the location denoted as red dot in (b)] from device 2.

Supporting Information S2

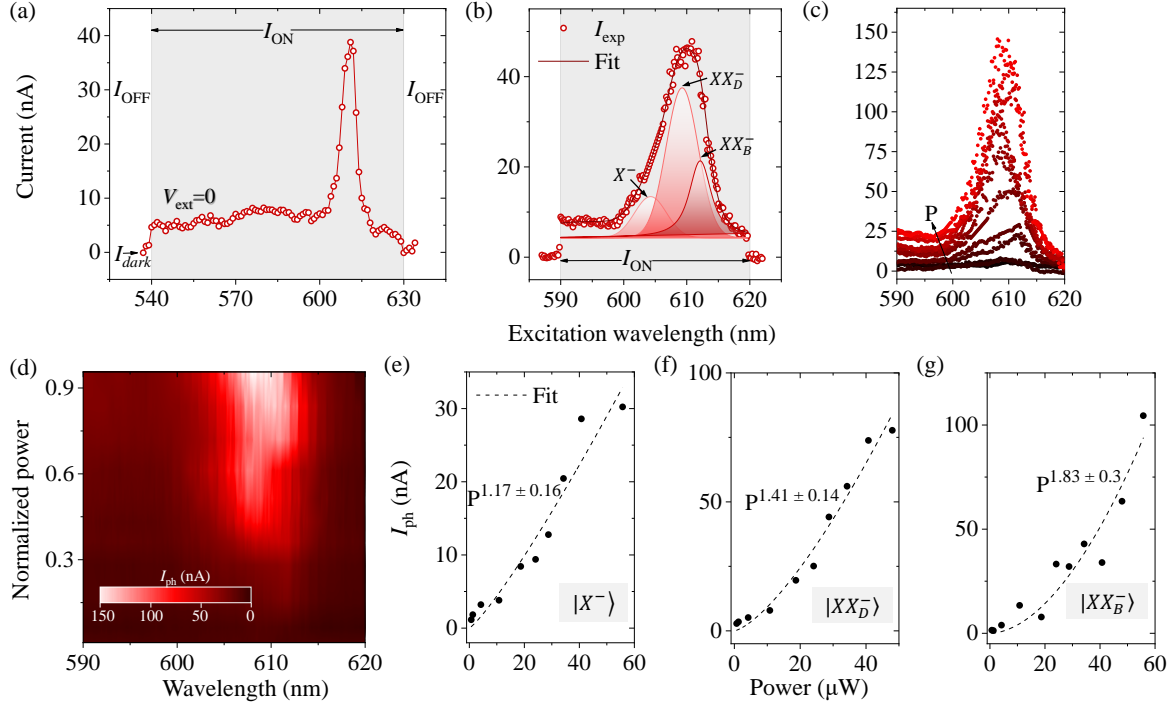


Figure 2: **Photocurrent (I_{ph}) from device-2.** (a) The photocurrent spectroscopic response of the device. The shaded region represents the ON current (I_{ON}) at zero external bias within the spectral range of $\lambda = 540 - 630$ nm. (b) Photocurrent spectral envelop (shown in open symbol) is decomposed into different energy states as X^- , XX_D^- and XX_B^- . (c) I_{ph} as function of increasing power (P) within the spectral range shown in b. (d) 2-D color plot of the I_{ph} within the spectral range. (e-g) Plot of I_{ph} power law for the X^- , XX_D^- and XX_B^- states in (e), (f) and (g) respectively. The dashed lines correspond to the fit of $I_{ph} \propto P^\alpha$. The α values are in good agreement with the device-1.

Supporting Information S3

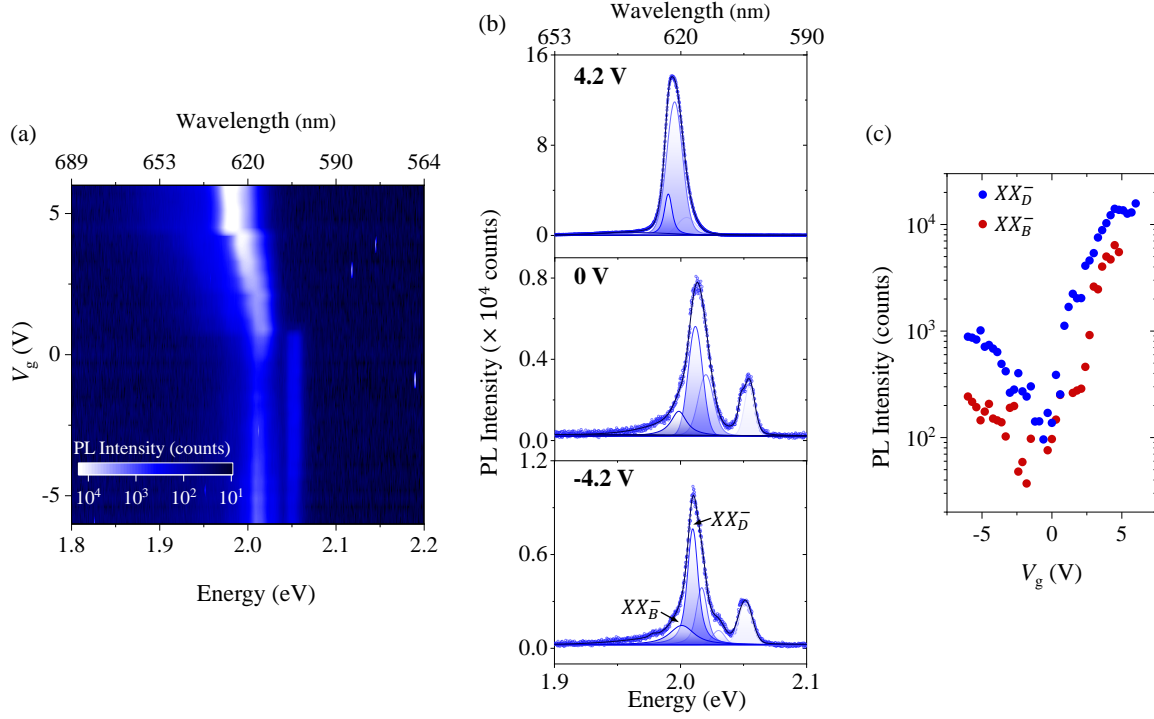


Figure 3: **Gate dependent photoluminescence of 1L-WS₂ at $T = 4.5$ K.** (a) color plot of the gate dependent PL intensity of 1L-WS₂ at $T = 4.5$ K. (b) Line cut of PL spectra at three different voltage points ($V_g = 4.2, 0, -4.2$ V). The spectra are further fitted with voigt function to extract the individual energy states (X^0 , X^- , XX_D^- and XX_B^-). While the X^0 peak is present at neutral region, it vanishes at the positive V_g or in the n -doped region. The $XX_{B,D}^-$ energy states are highly tunable across the doping regions. (c) PL intensity of the $XX_{B,D}^-$ state extracted from the fitting shown in b. The intensity tunability with gate voltage confirms the charged nature of both the species.

Supporting Information S4

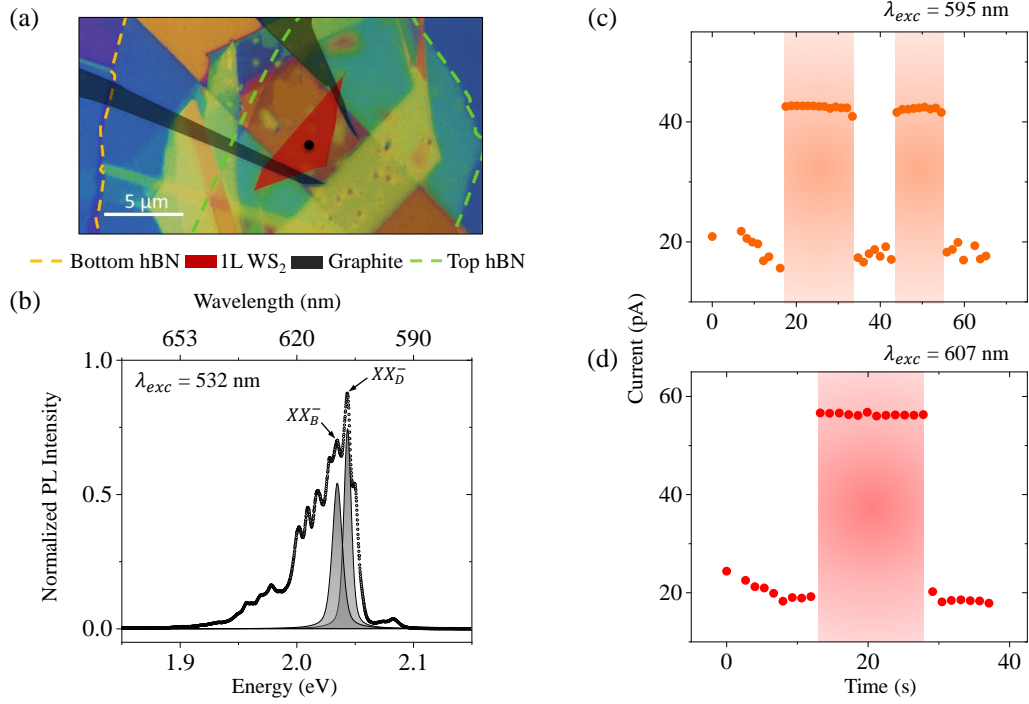


Figure 4: **Photoluminescence and photocurrent characteristics from a lateral device.**

(a) Optical image for the lateral device of 1L-WS₂ capped with hBN. (b) PL spectrum of hBN capped 1L-WS₂ at $T = 4.6$ K with 532 nm cw laser excitation. The fitting of the two charged biexcitons ($XX_{B,D}^-$) is shown for reference. (c-d) Current from the lateral device with excitation at (c) X^0 resonance ($\lambda_{exc} = 595$ nm) and (d) XX_D^- resonance ($\lambda_{exc} = 607$ nm) with $V_{ds} = 1$ V, and $T = 4.6$ K. The shaded and unshaded regions indicate light on and off, respectively. The corresponding I_{ph} is about 1000-fold lower compared to the vertical device described in the main text. In addition, there is no significant variation in I_{ph} observed upon resonant excitation at neutral exciton or charged biexciton.

Supporting Information S5

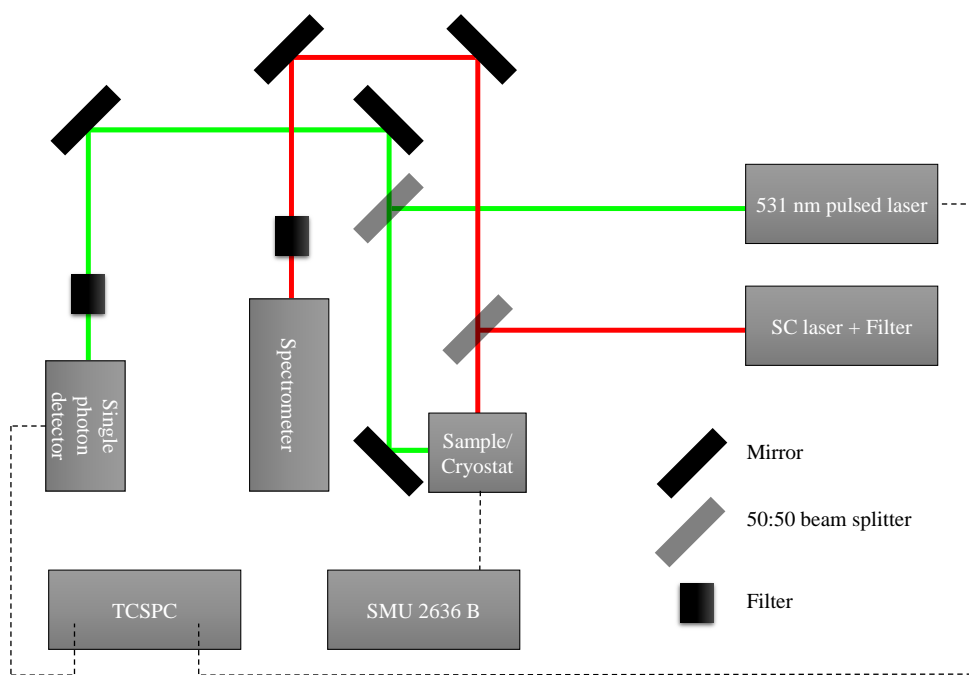


Figure 5: **Schematic of experimental setup.** Schematic diagram of the experimental setup used in photocurrent spectroscopy, PLE scan, and TRPL measurements.